Quantum Element Method for Multi-Dimensional Nanostructures Enabled by a Projection-based Learning Algorithm

Martin Veresko, Ming-Cheng Cheng*

Department of Electrical and Computer Engineering, Clarkson University, Potsdam, 13676, NY, USA

Abstract

A projection-based learning method developed previously based on proper orthogonal decomposition (POD), together with the quantum element method (QEM), is investigated for a 2D multi-element quantum nanostructure, where an element denotes a generic subdomain of a group of nanostructures. Unlike many other projection-based models, the basis functions for the POD approach are trained via solution data of the electron wave functions in the selected quantum state derived from direct numerical simulation of the Shcrödinger equation for the nanostructure. This learning process minimizes the least square error with a small set of basis functions to reduce computational effort. Based on the QEM, the nanostructures are first partitioned into smaller generic elements (i.e., building blocks), and each of the element is projected onto the POD space and stored in a database. For a large nanostructure, several generic elements can then be selected and glued together to perform simulation of the selected large nanostructure with the interface continuity imposed by the discontinuous Galerkin method. It has been shown that the QEM offers a reduction in numerical degrees of freedom (DoF) by 3 to 4 orders of magnitude for the trained quantum states with a high accuracy. For some untrained quantum states above the trained states, a reasonably accurate prediction can be achieved with higher DoF.

Keywords: quantum element method, proper orthogonal decomposition, quantum dots, wave function, data science

1. Introduction

Quantum nanostructures have many scientific and engineering applications in material sciences, medicine, electronics, photonics, etc. [1–8]. Analysis of such structures often rely on direct numerical simulations (DNSs) of the schrödinger equation which are computationally intensive when high accuracy and resolution are needed. This work continues the investigation on an effective quantum simulation methodology for electron wave functions (WFs) in multi-dimensional nanostructures [9]. This methodology employs proper orthogonal decomposition (POD) [10, 11] in which the schrödinger equation is projected onto a functional space represented by a finite set of basis functions (POD modes). Implemented with a learning algorithm trained via WF data, this approach is able to significantly reduce the degrees of freedom (DoF). One disadvantage of this approach however, is that it requires DNS WF data to generate/train the POD modes, which for large-scale multi-dimensional structures might be prohibitive.

To improve the training efficiency, this work implements the quantum element method (QEM), developed previously [12] for 1D quantum structures, in the POD simulation methodology for multi-dimensional nanostructures. The QEM combines domain decomposition with the POD training, allowing for the creation of modular generic elements which can be trained and stored in a database for the design and simulation of large nanostructures.

2. Background of Quantum Element Method

The electron WF is described by the Schrödinger equation,

$$\nabla \cdot \left[-\frac{\hbar^2}{2m^*} \nabla \psi \right] + U\psi = E\psi, \tag{1}$$

where ψ is the electron WF, $\hbar$ is the reduced plank constant, m^* is the electron effective mass, U is the potential energy of the system and E is the QS energy.

POD generates a set of modes $\eta(\vec{r})$, from the WF solution data generated via DNS of the Schrödinger equation. Each POD mode is created by maximizing its mean square inner product with the data,

$$\left\langle \left(\int_\Omega \psi(\vec{r}) \eta(\vec{r}) d\Omega \right)^2 \right\rangle \Big/ \int_\Omega \eta(\vec{r})^2 d\Omega. \tag{2}$$

Using calculus of variation, the maximization process can be reformulated to a Fredholm equation of the second kind,

$$\int_{\Omega'} \left\langle \psi(\vec{r}) \otimes \psi(\vec{r}') \right\rangle \vec{\eta}(\vec{r}') d\Omega' = \lambda \vec{\eta}(\vec{r}), \tag{3}$$

where $\otimes$ is the tensor operator and λ is the POD eigenvalue of the data. After generating the POD modes, the WF can be

*Corresponding author

Email addresses: vereskm@clarkson.edu (Martin Veresko), mcheng@clarkson.edu (Ming-Cheng Cheng)

formed via a linear combination of these POD Modes,

$$\psi(\vec{r}) = \sum_{j=1}^{M} a_j \eta_j(\vec{r}), \tag{4}$$

where M is the number of modes selected and a_j are weighting coefficients. To determine a_j, a set of equations can be found by projecting the Schrödinger equation onto each POD mode,

$$\begin{aligned} &\int_\Omega \nabla\eta_i(\vec{r}) \cdot \frac{\hbar^2}{2m^*} \nabla\psi(\vec{r}) d\Omega + \int_\Omega \eta_i(\vec{r}) U(\vec{r}) \psi(\vec{r}) d\Omega \\ &- \int_S \eta_i(\vec{r}) \frac{\hbar^2}{2m^*} \nabla\psi(\vec{r}) \cdot \hat{n} dS = E \int_\Omega \eta_i(\vec{r}) \psi(\vec{r}) d\Omega \end{aligned} \tag{5}$$

Using the QEM for a multi-element domain, elements are *glued* together with the interior penalty discontinuous Galerkin (DG) method [13, 14] to ensure interface continuity. The pth element projected along the ith mode described by (5) therefore becomes

$$\begin{aligned} \sum_{j=1}^{M_p} (T_{\eta_p,ij} + U_{\eta_p,ij}) a_{p,j} + \sum_{q=1,q\neq p}^{N_{el}} \sum_{j=1}^{M_p} B_{p,pq,ij} a_{p,j} + \\ \sum_{q=1,q\neq p}^{N_{el}} \sum_{j=1}^{M_p} B_{pq,ij} a_{q,j} = E a_{p,i}, \end{aligned} \tag{6}$$

where M_p and M_q are the number of modes in the pth and qth elements [12]. Additionally, the entries of the interior kinetic energy matrix for the pth element is found to be

$$T_{\eta_p,ij} = \int_{\Omega_p} \nabla\eta_{p,i} \cdot \frac{\hbar^2}{2m_p^*} \nabla\eta_{p,j} d\Omega, \tag{7}$$

the entries of the potential energy matrix are

$$U_{\eta_p,ij} = \int_{\Omega_p} \eta_{p,i} U \eta_{p,j} d\Omega, \tag{8}$$

the entries of the diagonal boundary kinetic energy matrix are

$$\begin{aligned} B_{p,pg,ij} = &-\frac{1}{2} \int_{S_{pq}} \frac{\hbar^2}{2m_p^*} \left[(\nabla\eta_{p,i}) \eta_{p,j} + \eta_{p,i} (\nabla\eta_{p,j}) \right] \eta_{p,i} \cdot d\vec{S} \\ &+ \mu \int_{S_{pq}} \frac{\hbar^2}{2m_p^*} \eta_{p,i} \eta_{p,j} dS, \end{aligned} \tag{9}$$

and the entries of the off diagonal boundary kinetic energy matrix are expressed as

$$\begin{aligned} B_{pg,ij} = &\frac{1}{2} \int_{S_{pq}} \frac{\hbar^2}{2m_p^*} \left[(\nabla\eta_{p,i}) \eta_{q,j} + \eta_{p,i} (\nabla\eta_{q,j}) \right] \eta_{p,i} \cdot d\vec{S} \\ &- \mu \int_{S_{pq}} \frac{\hbar^2}{2m_p^*} \eta_{p,i} \eta_{q,j} dS. \end{aligned} \tag{10}$$

In the above equations, μ is the penalty parameter defined as $\mu = N_\mu / dr$ where dr is the local mesh size at the interface and N_μ is the non-unit penalty number.

3. Materials and Structures

The QEM (namely the multi-element quantum POD approach) is applied to the test nanostructure seen in Fig. 1(a) composed of 4 elements with imposed homogeneous Dirichlet and Newman boundary conditions. The quantum dots (QDs) are composed of the GaAs/InAs heterostructure where the effective mass in GaAs $m^*_{GaAs} = 0.067 m_0$ and in InAs $m^*_{InAs} = 0.023 m_0$ and the band offset $\Delta E = 0.544 eV$. The POD modes for these elements are trained by collecting WF data after subjecting two 9-element training structures shown in Fig 1(b) with single component electric fields. In addition to an unbiased sample, two groups of orthogonal electric fields in x and y directions are applied to the training structures where 5 fields are applied in each direction.The magnitudes of these electric fields vary evenly between -35kv/cm and +35kv/cm. In each case, the WFs of the first 6 QSs were collected and used to train the POD modes for each element. This is accomplished via the method of snapshots [15–17] for (3) to generate the POD modes that are then used to evaluate the coefficients in (7)-(10).

4. Results and Discussions

The test nanostructure given in Fig. 1(a) is used for the demonstration of the multidimensional QEM. The structure is subjected to an electric field with x and y components, $\vec{E} = 25\hat{x} - 15\hat{y}$. After the training using two 9-element structures, as stated in Sec. 3 where only the first 6 QS WFs are collected, the QEM is used to predict the WFs for the first 8 QSs. These results are then compared to those of the DNS of the Schrödinger equation to verify the POD simulation model. The DNS control uses a grid size of 0.2nm in both x and y directions, thus resulting in 90601 DoF. In the POD simulation, $N_\mu = 2$ is selected for the penalty number in (9) and (10).

The profile and contour plots given in Figs. 2 and 3, respectively, reveal that the POD QEM agrees with the DNS quite well with 8 modes per element for the trained 6 QSs. It is interesting to observe in Fig. 2 that only 2 and 4 modes for each element in the QEM are needed in QSs 1 and 2, respectively, to offer a good accuracy compared to the DNS results; however, 8 modes are needed to reach a good accuracy for QSs 4 and 6.

To observe the influence of the POD modes on the QEM accuracy, the LS error is illustrated in Fig. 4 as a function of the number of modes per element. For the QEM to reach an LS error near or below 2%, 2, 4, 8, 8, 8 and 8 modes are needed in QSs 1-6, respectively. With an error near 2%, the POD and DNS WF profiles are nearly indistinguishable, as shown in Fig. 2. The maximum LS error for all the trained states is near 1.2% beyond 13 modes per element. In general, the POD model is more effective for the lower QSs. For the untrained states, the LS error is slightly larger. In the 7th QS, 4.9%, 4.3% and 3.8% are observed when 13, 19 and 22 modes are included in each element. However, for the 8th state, an LS error near 3.4% or below 3%, can be reached when using 10 or 16 modes, respectively.

The comparison of the eigenenergy in each QS between the POD and DNS is included in Tab. 1. The deviation of the POD

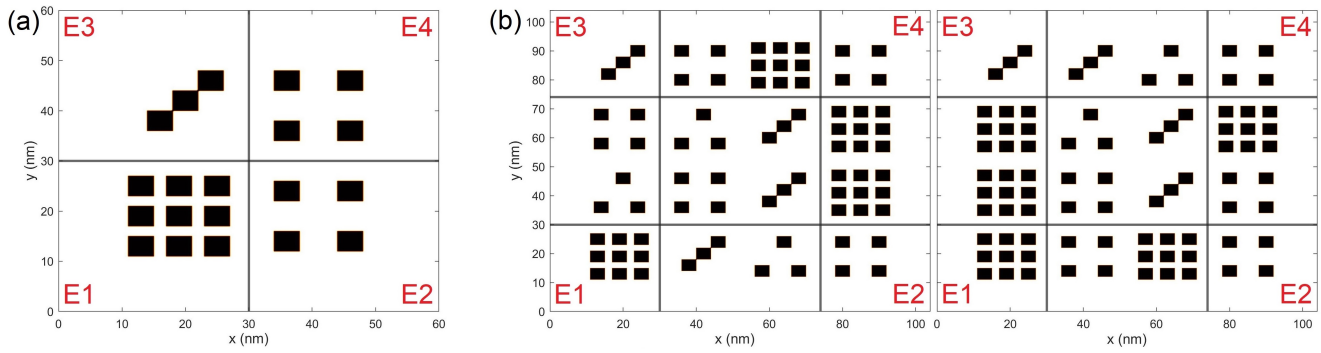

Fig. 1. (a) A 4-element structure for demonstration of QEM and (b) two 9-element structures for WF data collection.

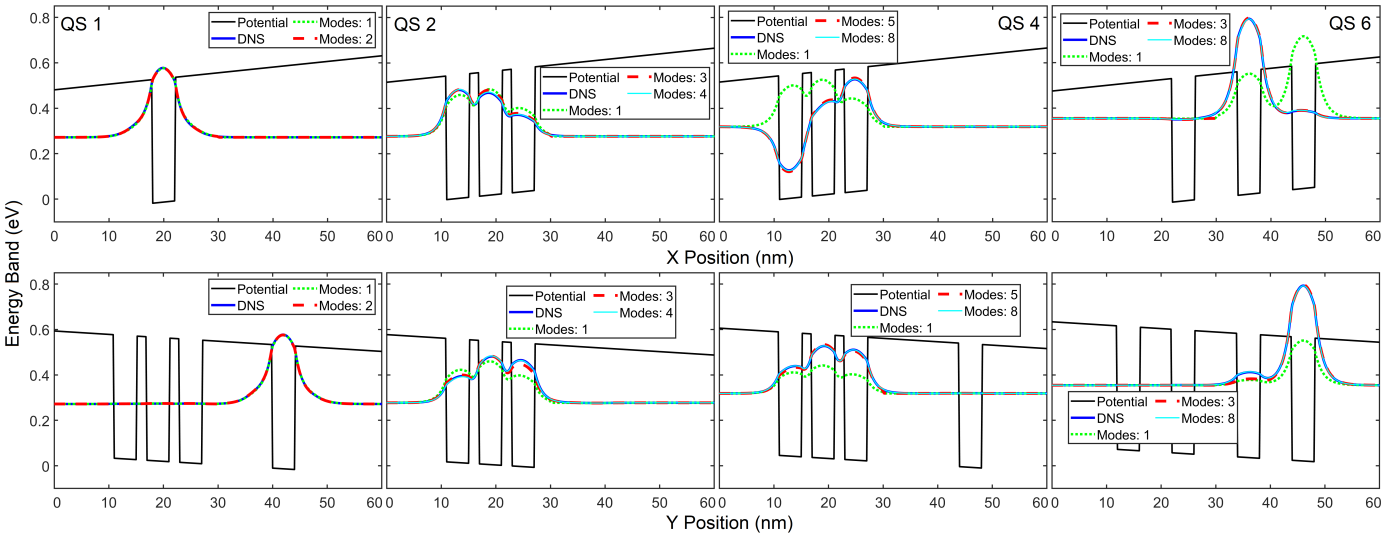

Fig. 2. WF Profile plots of QSs 1, 2, 4 and 6. First and second rows indicate cross-section along horizontal and vertical lines, respectively, indicated from contour plots seen in Fig. 3.

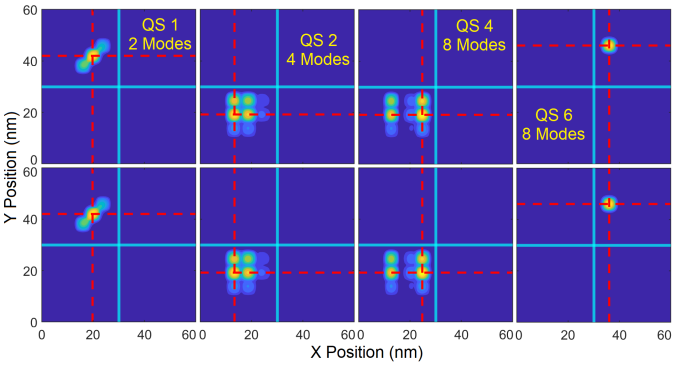

Fig. 3. Contour plot of WFs of QSs 1, 2, 4 and 6. First row are WFs calculated via POD while WFs in the second row are from DNS.

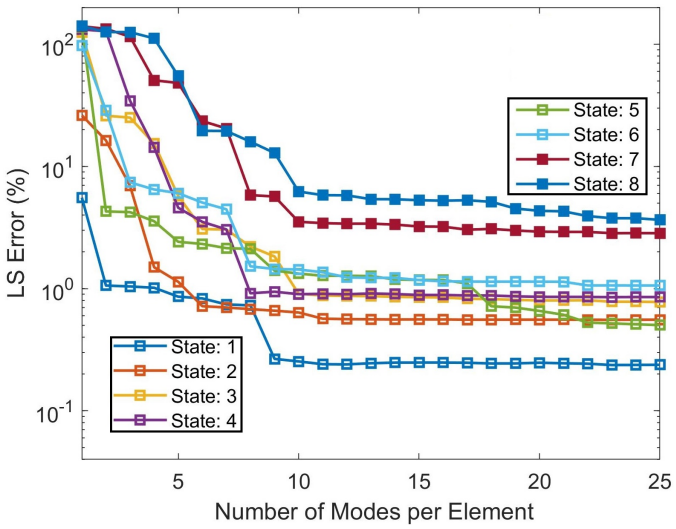

Fig. 4. LS Error Plot of WFs of first 8 QSs

eigenenergy from that of the DNS is less than 0.68% in QSs 1-7, where QS 7 is not trained. For the other untrained state, QS 8, the error of the POD eigenenergy is still as small as 0.83%. It should be noted that QSs 3 and 4 are nearly degenerate with a small energy difference of 2.35meV and 2.32meV from DNS and the POD QEM respectively.

It is worthwhile to mention that the training of POD modes was carried out separately in 2 orthogonal directions, and yet the QEM is able to predict the WFs and eigenenergies with a high accuracy using an electric field that combines these 2 orthogonal fields. In addition, even though WF data for States 7 and 8 were not collected for the training of POD modes, the QEM is still able to offer the WF solution and eigenenergy in these 2 states with a good accuracy.

Tab. 1. Percentage Error of Eigenenergy in Each State

QS	POD Energy (eV)	DSN Energy (eV)	(%) Difference
1	0.29888	0.29701	0.62631
2	0.30360	0.30229	0.43295
3	0.34313	0.34119	0.56768
4	0.34545	0.34354	0.55297
5	0.35336	0.35097	0.67970
6	0.38199	0.37969	0.60448
7	0.38521	0.38263	0.67287
8	0.39698	0.39371	0.82581

5. Conclusion

The QEM has been investigated for a 2D multi-element QD structure. It has been illustrated that the QEM is able to provide an accurate prediction of both the WF and eigenenergy in each of the trained QSs with 2 to 8 modes per element. In general, a similar accuracy can be reached with a smaller number of modes in the lower QSs. The investigation has demonstrated a reduction of 3 to 4 orders of magnitude in the required numerical DoF for the trained QSs, compared to the DNS. For the untrained QSs in the test QD structure, the QEM offers a good prediction with more modes. Moreover, POD training with single components of orthogonal electric fields is sufficient to develop a POD simulation approach for an electric field constructed using these 2 orthogonal components.

Acknowledgments

This work is supported by National Science Foundation under Grant Nos. OAC-1852102 and OAC-2118079.

References

[1] A. Andronov, E. Dodin, D. Zinchenko, Y. N. Nozdrin, Transport in gaas/al x ga1- x as superlattices with narrow minibands: Effects of interminiband tunneling, Semiconductors 43 (2) (2009) 228–235.

[2] S. A. Tatulian, From the wave equation to biomolecular structure and dynamics, Trends in biochemical sciences 43 (10) (2018) 749–751.

[3] A. J. Cohen, P. Mori-Sánchez, W. Yang, Insights into current limitations of density functional theory, Science 321 (5890) (2008) 792–794.

[4] H.-S. Zhang, L. Shi, X.-B. Yang, Y.-J. Zhao, K. Xu, L.-W. Wang, First-principles calculations of quantum efficiency for point defects in semiconductors: The example of yellow luminance by gan: Cn+ on and gan: Cn, Advanced Optical Materials 5 (21) (2017) 1700404.

[5] H. Dakhlaoui, J. Vinasco, C. Duque, External fields controlling the nonlinear optical properties of quantum cascade laser based on staircase-like quantum wells, Superlattices and Microstructures 155 (2021) 106885.

[6] G. J. Supran, K. W. Song, G. W. Hwang, R. E. Correa, J. Scherer, E. A. Dauler, Y. Shirasaki, M. G. Bawendi, V. Bulović, High-performance shortwave-infrared light-emitting devices using core–shell (pbs–cds) colloidal quantum dots, Advanced Materials 27 (8) (2015) 1437–1442.

[7] S. A. Veldhuis, P. P. Boix, N. Yantara, M. Li, T. C. Sum, N. Mathews, S. G. Mhaisalkar, Perovskite materials for light-emitting diodes and lasers, Advanced materials 28 (32) (2016) 6804–6834.

[8] F. P. García de Arquer, D. V. Talapin, V. I. Klimov, Y. Arakawa, M. Bayer, E. H. Sargent, Semiconductor quantum dots: Technological progress and future challenges, Science 373 (6555) (2021) eaaz8541.

[9] M. Veresko, M.-C. Cheng, An effective simulation methodology of quantum nanostructures based on model order reduction, in: 2021 International Conference on Simulation of Semiconductor Processes and Devices (SISPAD), IEEE, 2021, pp. 64–68.

[10] J. L. Lumley, The structure of inhomogeneous turbulent flows, Atmospheric turbulence and radio wave propagation (1967).

[11] J. L. Lumley, Stochastic tools in turbulence, Courier Corporation, 2007.

[12] M.-C. Cheng, Quantum element method for quantum eigenvalue problems derived from projection-based model order reduction, AIP Advances 10 (11) (2020) 115305.

[13] D. N. Arnold, F. Brezzi, B. Cockburn, D. Marini, Discontinuous galerkin methods for elliptic problems, in: Discontinuous Galerkin Methods, Springer, 2000, pp. 89–101.

[14] D. N. Arnold, F. Brezzi, B. Cockburn, L. D. Marini, Unified analysis of discontinuous galerkin methods for elliptic problems, SIAM journal on numerical analysis 39 (5) (2002) 1749–1779.

[15] L. Sirovich, Turbulence and the dynamics of coherent structures. i. coherent structures, Quarterly of applied mathematics 45 (3) (1987) 561–571.

[16] W. Jia, B. T. Helenbrook, M.-C. Cheng, Fast thermal simulation of finfet circuits based on a multiblock reduced-order model, IEEE Transactions on Computer-Aided Design of Integrated Circuits and Systems 35 (7) (2015) 1114–1124.

[17] W. Jia, M.-C. Cheng, A methodology for thermal simulation of interconnects enabled by model reduction with material property variation, Journal of Computational Science 61 (2022) 101665.